Available online at www.sciencedirect.com

ScienceDirect

Energy Procedia 00 (2015) 000–000

Energy Procedia

www.elsevier.com/locate/procedia

International Conference on Concentrating Solar Power and Chemical Energy Systems, SolarPACES 2014

An exergy analysis of tubular solar-thermal receivers with different working fluids

J. Pye[1], M. Zheng, C.-A. Asselineau and J. Coventry

Australian National University, Research School of Engineering, Canberra, Australia

Abstract

Tubular solar thermal receivers suitable for central towers are modelled using energy and exergy analysis, in a way that allows individual inspection of the the irreversibilities associated with the various receiver heat transfer processes occurring. The model was used to compare the behaviour of four working fluids: molten salt (NaNO3/KNO3), liquid sodium metal, supercritical carbon dioxide, and ideal air. In the working fluid temperature range 300–550 °C, the model showed sodium and molten salt to be the best performers. At elevated temperature ranges, sodium and carbon dioxide become the preferred candidates. The biggest differences in exergy terms between the alternative fluids are in exergy loss by thermal emission, and in the exergy destruction associated with internal convection losses and wall conduction.

Peer review by the scientific conference committee of SolarPACES 2014 under responsibility of PSE AG.

Keywords: exergy receiver, central tower, losses, thermodynamics.

1.Introduction

Tubular receivers are dominant across almost all CSP receivers in large-scale use, whether for trough, linear Fresnel, dish/Rankine [1] or tower configurations [2]. In this paper, we seek to assess how different choices for working fluids in the receiver impact on the thermal performance, by comparing the exergetic efficiency of receivers of these different types, and determining where the major sources of exergy destruction occur, using somewhat simplified heat transfer modelling. The selected working fluids for the comparison are molten nitrate salt, liquid sodium, supercritical carbon dioxide (sCO2) and air.

The analysis follows a similar approach to previous works [3-5] but is specific to central tower receivers, and adds an exergy analysis with the different sources of irreversibility kept separate, as as a tool for comparison and for examination of the trade-offs between the different fluids.

[1] Corresponding author. Tel.: +61 2 6125 8778
E-mail address: john.pye@anu.edu.au

Peer review by the scientific conference committee of SolarPACES 2014 under responsibility of PSE AG.

Nomenclature

h	convection coefficient *or* specific enthalpy	T	temperature
Q	heat rate	X	exergy rate
ϕ	specific flow exergy	α	absorptivity, solar-weighted
ϵ	emissivity	σ	Stefan-Boltzmann constant
n_{tubes}	number of tubes per bank	n_{banks}	number of tube banks in the receiver
n	number of flow segments in the receiver	G	direct normal irradiance
C	concentration ratio	L	length (along receiver tube)
k	thermal conductivity	Nu	Nusselt number
Re	Reynolds number	Pr	Prandtl number
f	Friction factor	ρ	density
V	flow velocity (bulk)	η	efficiency
$\dot{m}$	mass flow rate	Δp	pressure drop through receiver

Subscripts

refl	reflected	sun	incident solar *or* sun
abs	absorbed	rad	radiation due to thermal emission
ext	external wall of receiver tube	int	internal wall of receiver tube
slice	for/in one flow segment only	dest	destroyed within the system
lost	lost through leaving the system	i	transferred to the working fluid
i	flow segment index	ref	exergy reference condition
I	first law	II	second law
conv	convective heat transfer		

2.Model description

The receiver to be modelled in this paper is a Gemasolar-style receiver with convex banks of vertical tubes arranged to face the solar field (Figure 1). The total receiver surface is 100 m², and assumed fixed. The flow path is discretised into a specified number of flow segments (n), and there are n_{banks} passes up and down the receiver surface. The number of parallel tubes in each bank, n_{tubes} can then be calculated on an area basis knowing outside diameter d_{ext} of the tubes in question. The receiver surface area is assumed to be entirely packed with tubes; no allowance has been made for thermal expansion at this stage. The incidence flux from the solar field is assumed to be uniform over the entire receiver surface at 1500 suns, with a direct normal irradiance of 800 W/m² assumed; this highly simplifying assumption will be discussed later in the paper.

Receiver tubes are assumed to have been coated with Pyromark 2500® paint, which was characterised for solar receiver applications by Ho et al [6]. Ho et al found that the emissivity of Pyromark increases from ~0.86 at 300°C to 0.88 at 550°C and to 0.90 at 1000°C. Operation of Pyromark at elevated temperatures (>750°C) may lead to degraded performance, but this has not been considered in this model.

For each flow segment, external radiative flux, thermal emission, external convection, wall conduction, internal convection and flow friction are considered, leading to an overall mass, energy, and momentum balance for each segment. The correlations and equations used for each of these will be described below. The flow per segment is determined from the total receiver mass flow divided by n_{tubes} ; the total losses can be determined by taking the losses from a single tube-path through the receiver and again multiplying by n_{tubes} . The effect of entry and exit manifolds, minor losses, etc are so far not considered.

Exergy losses associated with each of the heat and mass transfer phenomena are are calculated, and then summed to determine a breakdown of exergy losses by phenomenon.

The aim of this paper is to compare receivers on two bases. Firstly, to compare recievers with different working fluids, but optimised for the same temperature range of 300 °C to 550 °C. This comparison seems to highlight performance differences intrinsic to the fluid as a result of its thermophysical properties and those the associated

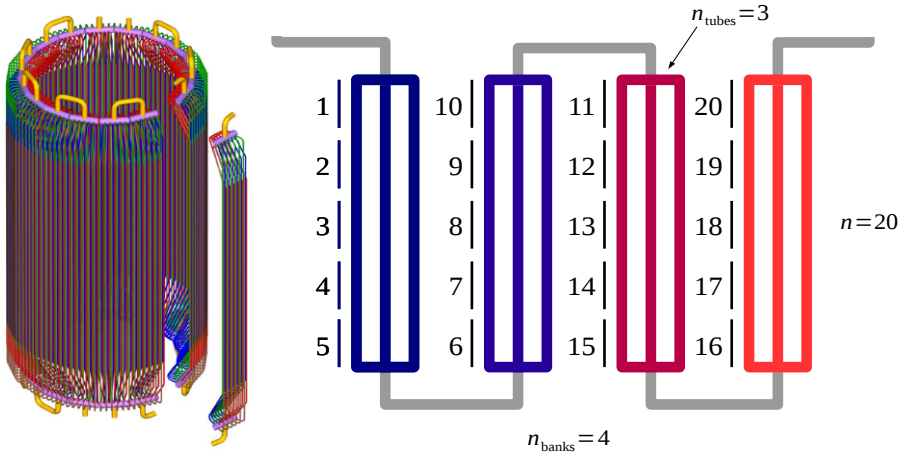

Figure 1. Billboard receiver (Source: ISE, Univ Carlos III), and receiver pipe flow model numbering and layout.

pipework needed to hold it. Secondly, we compare receivers with different working fluids and with a temperature range considered to be realistic and technically feasible, given anticipated material limits. This second comparison aims to quantify the gains that can be made with different receivers when the various issues of downstream storage and power cycles, etc., are overcome. The comparison is predominantly on the basis of exergy destruction, and hence the benefits of higher outlet temperature (leading to higher power cycle inlet temperature) are inherently included in the analysis.

The same essential receiver model is used for each of the heat transfer fluids of interest. In each case, suitable heat transfer correlations and fluid properties data are required. Once an initial design for a fluid of interest is found, the design is coarsely optimised by adjusting the number of tube banks and number of tubes. These variables are highly sensitive to the working fluid chosen, as will be seen below.

2.1. Fluid properties

For molten nitrate salt (60% NaNO3, 40% KNO3), incompressible fluid is assumed. The temperature-dependent density, specific heat capacity, dynamic viscosity and thermal conductivity are taken from Zavoico [7]. The incompressible fluid assumption is applied in order to generate expressions for enthalpy and entropy.

For liquid sodium, property correlations from Fink and Liebowitz [8] were used, again assumed incompressible.

For supercritical carbon dioxide, the Span and Wagner Helmholtz equation of state [9] is used, with viscosity [10] and thermal conductivity [11] correlations. The correlations are implemented in the FPROPS properties code.

For air, the ideal gas assumption is used, together with the viscosity correlation of Lo et al. [12] and the conductivity correlation of Kadoya et al [13]. Some discrepancy arises in calculation of these thermophysical properties from the use of the ideal gas equation of state, but this was checked against REFPROP [14] and found to be less than ±4% for temperatures close to 300°C, and less than ~±1% for higher temperatures. Air property calculations relating to external convection losses were determined by cubic spline interpolation from the table of air properties at ambient pressure of Holman [15].

It is believed that the accuracy of the fluid properties data used here is high enough to allow some quantitative comparison of receiver configurations, although it may not be sufficient for a detailed design process.

2.2. External heat transfer

For this study, we model absorption of uniform concentrated solar flux, together with thermal emission as a simple function of pipe outer-wall temperature, and natural convection heat losses, in both cases for only the outward-facing half of the tube, $A_{\text{ext,slice}}=\frac{1}{2}\pi d_{\text{ext}} L_{\text{slice}}$.

The total absorbed solar radiation in the receiver is $Q_{\text{abs}} = \alpha C G A_{\text{apert}}$, giving $Q_{\text{abs,slice}} = Q_{\text{abs}} / n_{\text{tubes}} / n$ as the solar radiation absorbed on each flow segment. From Ho et al [6], the mto be 0.967, but has been reduced to 0.95 to allow for the effects of surface aging. The effective absorptivity is further adjusted to allow for the small amount of re-absorption of scattered/reflected radiation that will occur in the crevices between tubes. The result is that the effective absorptivity of the tube bank on a per-aperture-area basis increases again to 0.968.

Thermal emission losses for the external surface are calculated from the convex-surface-in-large-enclosure equation, $Q_{\text{ext,rad}} = \epsilon \sigma A_{\text{ext,slice}} \left(T_{\text{ext}}^4 - T_{\text{amb}}^4 \right)$.

A temperature-dependent emissivity value $\epsilon(T)$ is calculated locally for the external tube temperature. A curve-fit was made from the plotted data of Ho et al [6] for Pyromark on cold-rolled steel at 600°C, giving emissivity as a function of temperature in kelvin:

$$\epsilon(T) = 0.1477 \log_e (T - 264.6\,\text{K}) - 5.671 \times 10^{-6} (T - 264.6\,\text{K})^{1.3078} + 0.4988 .$$

The 'sky' temperature is assumed to be equal to the ambient air temperature for this simple analysis. Also, there is no allowance made the effective emissivity of the tube bank to consider the non-convex nature of the surface, and the entire outward-facing tube area is used for the thermal emission calculation. It is again noted that a uniform flux assumption is applied here, which will have the effect of reducing the calculated thermal emission losses compared to the real case with varying flux. Further accuracy in the thermal emission loss model requires a locally-varied flux model, which is planned as future work.

External convection heat transfer is considered to occur with a fixed-value convection heat transfer coefficient h_{ext} of 30 W/m²K. This value was chosen for consistency with the earlier comparative analysis of Boerema et al [16]. An evaluation of the convection coefficient by natural convection alone, using the vertical wall correlation of Churchill and Chu as given in Incropera and Dewitt [17], gives a significantly lower value of 6.9 W/m²K, so it can be concluded that the selected h_{ext} value makes some limited allowance for the effect of wind, but that a detailed analysis (such as that of Zanino et al [18]) would be needed to quantify it more precisely. Using the assumed value of convection coefficient, the convection losses are $Q_{\text{ext,conv}} = h_{\text{ext}} A_{\text{ext,slice}} \left(T_{\text{ext}} - T_{\text{amb}} \right)$.

2.3. Wall conduction

Wall conduction is assumed to be radial only through just the outward facing half of the pipe:

$$Q_{\text{i}} = \frac{1}{2} \frac{2\pi k L_{\text{slice}} \left(T_{\text{ext}} - T_{\text{int}} \right)}{\ln \left(d_{\text{ext}} / d_{\text{int}} \right)} .$$

Rodríguez-Sánchez et al. [5] noted that circumferential wall heat fluxes can be expected to be two orders of magnitude less than those in the radial direction, and that they can be ignored for molten-salt receiver designs. The validity of that assumption was not tested for the other fluids in the present study; it is possible that for high-pressure receivers with thick walls and lower internal convection coefficients, then circumferential conduction could play a more significant role.

2.4. Internal convection

Internal convection heat transfer is calculated using standard internal flow forced convection correlations, but the heat transfer area is assumed to be half: only the front half of the pipe. Using published correlations in this way will be approximate at best, as the non-uniform wall temperature profile will certainly affect the flow profile, and introduce discrepancies in convective heat transfer compared to the uniform wall temperature case that the correlations are based on.

For molten salt, air, and supercritical CO2, the Dittus-Boelter equation, as given by Incropera and DeWitt is used [17], with properties evaluated at the working fluid bulk temperature T,

$$\text{Nu}_{\text{int}} = 0.023\,\text{Re}^{0.8}\,\text{Pr}^{0.4} .$$

Various correlations are available for calculation of supercritical fluid internal forced convection heat transfer, as reviewed by Cheng and Schulenberg [19], however such correlations are not used here. They found the discrepancy between supercritical correlations and the Dittus-Boelter be quite large, but only in the vicinity of ~±20°C near the critical point. The conception sCO2 receiver in this study operates over a far wider temperature range, so the inaccuracy due to the use of Dittus-Boelter was considered tolerable for an initial comparison.

For liquid sodium, the Lyon-Martinelli correlation, as quoted by Pacio et al [20] is used,

$$\mathrm{Nu}_{\mathrm{int}} = 7.0 + 0.025\left(\mathrm{Re}\,\mathrm{Pr}\right).$$

The resulting heat transfer is calculated using $h_{\mathrm{int}} = \mathrm{Nu}_{\mathrm{int}}\, k / d_{\mathrm{int}}$ and $Q_{\mathrm{i}} = h_{\mathrm{int}} A_{\mathrm{int,slice}} \left(T_{\mathrm{int}} - T\right)$.

2.5. Pressure drops

Frictional pressure drop is calculated using the Darcy friction factor f,

$$\left(\Delta p\right)_{\mathrm{fric}} = -f \frac{1}{2} \rho \mathbf{V}^2 \frac{L_{\mathrm{slice}}}{d_{\mathrm{int}}}.$$

For this study, we assume smooth pipes and turbulent flow, so the Petukhov equation, as given by Bergman et al [21] is used to calculate friction factor: $f = \left(0.790 \ln\left(\mathrm{Re}\right) - 1.64\right)^{-2}$. Minor losses have not been considered. The model also ignores the unheated portion of pipework which would normally be present.

2.6. Flow segment model

Each flow segment has an inlet and an outlet, and energy and momentum balances are applied to relate the steady-state flow conditions to the incident flux and wall internal/external surface temperatures. The momentum balance is

$$p_{i+1} - p_i = \left(\Delta p\right)_{\mathrm{fric},i} - \left(\rho_{i+1} \mathbf{V}_{i+1}^2 - \rho_i \mathbf{V}_i^2\right).$$

The energy balance for the fluid flow is

$$\dot{m}\left[\left(h_{i+1} - h_i\right) + \frac{1}{2}\left(\mathbf{V}_{i+1}^2 - \mathbf{V}_i^2\right)\right] = Q_{\mathrm{i},i}.$$

The energy balance for the outer surface of the pipe wall is

$$Q_{\mathrm{abs,slice},i} = Q_{\mathrm{i},i} + Q_{\mathrm{ext,conv},i} + Q_{\mathrm{ext,rad},i}.$$

For the pipe wall, a factor of safety is calculated using a simple hoop stress calculation, and this factor of safety is required to remain above 1:

$$F_{safety} = \frac{2 t \sigma_{\mathrm{allow}}}{\pi d_{\mathrm{ext}}}.$$

An overall model is made by cascading multiple fluid segment models, and then iteratively solving the whole system, using the equation-based ASCEND modelling environment, and its standard QRSlv solver [23]. To generate a robust solution process, the system is first solved with a fixed inlet temperature and flow rate. Once solved, the outlet temperature is fixed and the model is solved again with flow rate as a free variable. The resulting flow-path solution yields heat fluxes that must be multiplied by n_{tubes} to calculate corresponding values for the whole receiver.

The overall first-law efficiency of the receiver is

$$\eta_I = \frac{\sum Q_{\mathrm{i}}}{\sum Q_{\mathrm{sun}}}.$$

2.7. Exergy analysis

Exergy in incident sunlight is calculated by the Petela formula, as developed by Candau [22],

$$X_{\text{sun}} = Q_{sun}\left(1 - \frac{4}{3}\frac{T_{\text{ref}}}{T_{\text{sun}}} + \frac{1}{3}\left(\frac{T_{\text{ref}}}{T_{\text{sun}}}\right)^4\right).$$

A share of this exergy is lost in reflection, $X_{\text{refl}} = (1-\alpha) X_{\text{sun}}$. Of the solar exergy not reflected, αX_{sun}, some is successfully absorbed,

$$X_{\text{abs}} = Q_{\text{abs,slice}}\left(1 - \frac{T_{\text{ref}}}{T_{\text{ext}}}\right).$$

The rest of αX_{sun} is destroyed, partly due to the reduced temperature compared to the sun, and partly due to optical irreversibilities. In this paper, the relative importance of these two effects is not examined. Exergy transferred by conduction to the inner surface of the pipe is then

$$X_{\text{int}} = Q_{\text{i}}\left(1 - \frac{T_{ref}}{T_{\text{int}}}\right).$$

Exergy transferred to the working fluid by convection on the pipe is

$$X_{\text{conv}} = Q_{\text{i}}\left(1 - \frac{T_{\text{ref}}}{T}\right).$$

Exergy lost by convection and radiation is calculated from the exergy of $Q_{\text{ext,conv}}$ and $Q_{\text{ext,rad}}$ evaluated at the wall temperature:

$$X_{\text{loss,ext,conv}} = Q_{\text{ext,conv}}\left(1 - \frac{T_{\text{ref}}}{T_{\text{ext}}}\right), \quad \text{and} \quad X_{\text{loss,ext,rad}} = Q_{\text{ext,rad}}\left(1 - \frac{T_{\text{ref}}}{T_{\text{ext}}}\right).$$

We calculate the exergy lost due to flow friction indirectly, using the exergy balance of the fluid flowing through the flow segment, since the flow exergy takes into account the pressure changes arising from pipe friction,

$$X_{\text{dest,flow}} = X_{\text{conv}} + \dot{m}\left(\phi_{i-1} - \phi_i\right).$$

In all cases, the exergy is evaluated against the chosen reference conditions T_{ref} and p_{ref}. In the case of supercritical carbon dioxide, the reference conditions are below the triple-point pressure, making fluid property calculation more difficult. As a workaround, p_{ref} is chosen as 6 bar for the case of CO_2.

The outcome of this exergy accounting is shown in Figure 3, which includes values added up for all of the flow segments in the model. The quantities shown on this Sankey diagram are (1) X_{sun}, (2) X_{refl}, (3) destroyed in absorption, $X_{\text{dest,abs}} = X_{\text{sun}} - X_{\text{abs}}$, (3) $X_{\text{loss,ext,conv}}$, (4) $X_{\text{loss,ext,rad}}$, (5) destroyed in wall conduction, $X_{\text{dest,wall}} = X_{\text{abs}} - X_{\text{int}}$, (6) destroyed in internal convection $X_{\text{dest,int,conv}} = X_{\text{int}} - X_{\text{conv}}$, (7) carried in with the working

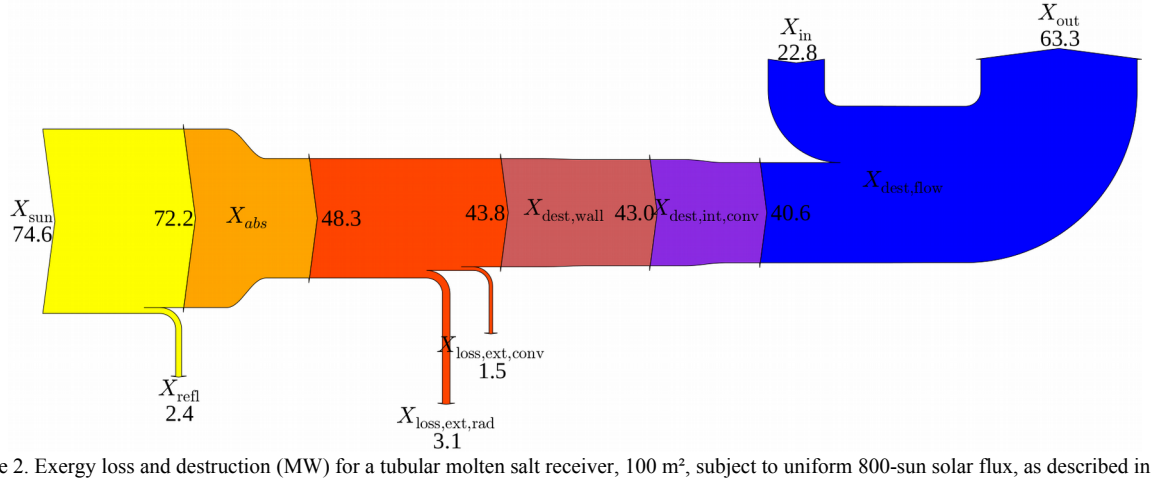

Figure 2. Exergy loss and destruction (MW) for a tubular molten salt receiver, 100 m², subject to uniform 800-sun solar flux, as described in §3.2.

fluid $X_{in} = \dot{m}\phi_{in}$ and (8) out $X_{out} = \dot{m}\phi_{out}$, and finally (9) the next gain in working-fluid exergy $X_{net} = X_{out} - X_{in}$. From this accounting, we define the exergy efficiency as

$$\eta_{II} = X_{net} / X_{sun} .$$

A key difference between exergy accounting and energy accounting is that exergy is destroyed when heat transfer occurs over a temperature difference. As a result, a major component of exergy destruction is the initial absorption step, described above. For high temperature surfaces, this destruction is lower; for lower-temperature surfaces, this destruction is higher.

Exergy accounting somehow reverses the usual thinking about CSP systems, where we see that most of the exergy is destroyed in the absorption step; in energy accounting we see most of the energy being lost in low-temperature heat rejection. It is important to bear this in mind when examining the following results.

3.Analysis and discussion

3.1. Validation

The receiver model was tested over a wide range of parameters, and exhibits qualitatively the expected physical behaviour. The overall first-law efficiency values are consistent with other works (such as [4, 5, 23]). The main aim of this paper however is to examine the relativities between different working fluids, and given the significant approximations, such as the assumption of uniform flux, so further detailed validation is not pursued here.

3.2. Case 1: fixed temperature limits.

Firstly, we compare the performance of receivers with different working fluids when operating at the identical temperature range of 300–550°C for each case. This range is chosen because it is close to the typical range of molten salt receivers (and conventional molten salt storage) and, furthermore, it is compatible with operating limits for all of the fluids being compared in this study. Parameters selected for the comparison are shown in Table 1. Fluid-specific parameters show values selected to maximise exergetic efficiency; the process of optimising these parameters was not exhaustive, and will be the subject of further work.

The results shown in Figure 3 and Table 1 show that the salt and sodium are very close in performance, with sodium having a slight advantage due to better internal convection, and knock-on benefits from lowered external losses. CO_2 performs a little worse, because of internal convection, and also the need for thicker pipe walls. Air, finally, performs quite poorly, due to extremely large convection temperature differences. Further work is needed to determine whether a better receiver design can alleviate this temperature difference while also not leading to large pressure drops.

Another observation, in relation to optimisation of the design parameters for Case 1, is that better performance could be achieved by making tubes smaller and smaller. The result was very large pressure drops across the receivers, especially for salt and sodium, but these pressure drops did not appear to have the expected impact on exergy efficiency. It is thought that this is (1) because of the incompressible fluid assumption used for property calculations for these fluids, and perhaps more importantly, (2) because pumping irreversibilities are not included within the exergy accounting.

This highlights the limitations of the present approach of identifying only the irreversibilities within the receiver itself. Although it is instructive to compare performance within the receiver, compressors, pumps, turbines and heat exchangers elsewhere in the system will be of major importance in the working fluid choice.

3.3. Case 2: operating limits according to material/fluid limits.

In Case 1, the molten salt receiver is already operating at high performance; its emissions and convective losses are moderate, and thermal stability considerations prevent high temperatures being considered. However, for the other fluids, higher temperatures are certainly possible. In this section, we investigate the way that the irreversibilities in the receiver change as temperature is increased (Table 2, Figure 4)

Table 1: Case 1 model parameters and results.

Common parameters (p_{ref} =6 bar for CO_2)

C	G	T_{sun}	A_{aper}	p_{ref}	T_{ref}	σ_{allow}	k_{wall}	α	T_{in}	T_{out}	h_{ext}
800	1000 W/m²	5800 K	100 m²	1 bar*	20 °C	100 MPa	20 W/m·K	0.95	300 °C	550 °C	30 W/m²K

Fluid-specific parameters and results

Fluid	L / [m]	n_{banks}	d_i / [cm]	p_o / [bar]	t / [mm]	$\dot{m}$ / [kg/s]	η_I	η_{II}	Δp / [bar]	$(T_{ext}-T_{int})_{i=0}$ / [K]	$(T_{int}-T)_{i=0}$ / [K]
molten salt	10	4	1.8	1	1	185	0.878	**0.542**	-4.2	24	86
sodium	10	1	2.0	1	1	224	0.896	**0.552**	-0.1	25	12
CO_2	10	2	2.2	220	4	213	0.828	**0.508**	-3.5	104	110
air	1.25	1	1.0	20	2	161	0.540	**0.325**	-0.1	34	576

Firstly, for liquid sodium, it is feasible to increase the maximum temperature to 850°C, which is safely below the boiling temperature while still allowing a safety-margin for locally-elevated film temperatures without the onset of boiling. Because efficient power cycles usually incorporate regeneration/preheating, we will also increase the inlet temperature up to 500°C. The now much hotter receiver is seen to have much larger external convective and radiative losses, and these have led the receiver efficiency to drop to 76.4%.

Secondly, for supercritical CO_2, we will increase to a temperature range from 500 to 700 °C.

For air, it seems impossible to increase the working temperature without the thermal emission losses becoming untenable. The example shows ever increasing thermal emission losses, due to poor convection which can not easily be improved without generating large pressure drops.

Another example in Case 2, we consider a quasi-cavity analysis, where the absorber is *half* the surface area of the cavity aperture. This is approximated by *reducing* the concentration ratio and *increasing* the absorber area, both by a factor of two. The emissivity can also be decreased by a factor of 2, to simulate the view-factor effect arising from the cavity. We assume a halving of the convection coefficient to 15 W/m²/K to account for the shielding provided by the cavity structure. At the level of analysis possible with this model, we see a slight improvement from the addition of the cavity.

Finally, we simulate the benefit of increased field performance. If the geometric concentration ratio can be doubled, though higher-quality heliostats, then the aperture area can be halved without changing the solar energy input. The result of this marked: improving field optics is clearly one of the best ways to improve receiver performance. The benefit arises from reduced area for emission and convection. The effect is slightly non-linear;

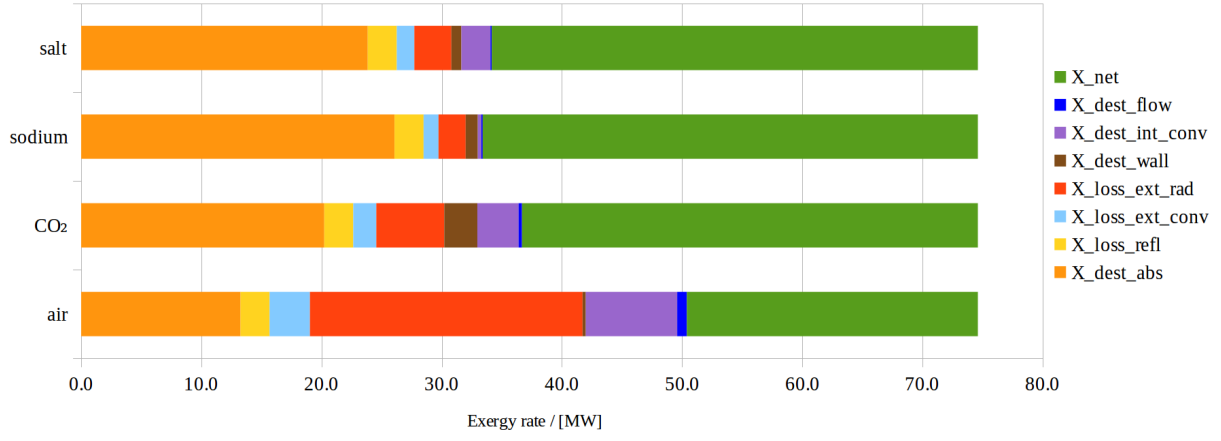

Figure 3. Case 1: exergy accounting for the comparison receivers, all operating with equal solar flux and equal 300–550°C working fluid temperature range. Sodium, with its excellent heat transfer characteristics has the best performance but only marginally better than salt. The gas receivers with air and CO_2 have greater internal convection losses, which lead to elevated external temperatures, and hence greater convective and radiative losses. Finally, CO_2 has large wall losses because of the thick wall required for the supercritical working pressures. Wall losses for air are very low because exergy destruction for conduction is smaller when it occurs in a higher temperature range.

Table 2: Case 2 model parameters and results.

Common parameters (p_{ref} =6 bar for CO_2)

C	G	T_{sun}	A_{aper}	p_{ref}	T_{ref}	σ_{allow}	k_{wall}	α	T_{in}	T_{out}	h_{ext}
800*	1000 W/m²	5800 K	100 m²*	1 bar*	20 °C	100 MPa	20 W/m·K	0.95	300 °C	550 °C	30 W/m²K*

Fluid-specific parameters and results

Fluid	L / [m]	n_{banks}	d_i / [cm]	p_o / [bar]	t / [mm]	$\dot{m}$ / [kg/s]	η_I	η_{II}	Δp / [bar]	$(T_{ext}-T_{int})_{i=0}$ / [K]	$(T_{int}-T)_{i=0}$ / [K]
sodium 500–850°C	10	1	0	1	1.0	139	0.764	**0.563**	-0.06	23	17
CO_2 500–700°C	10	2	0	220	2.5	245	0.772	**0.538**	-13.40	60	64
air 700–890°C	1	1	0	100	0.7	180	0.491	**0.381**	-0.14	11	219
sodium 500–850°C cavity C =400, A_{aper} =200 m², $\frac{1}{2}\epsilon$	10	1	0	1	1.0	141	0.773	**0.570**	-0.02	12	14
sodium 500–850°C high-flux C =1600, A_{aper} =50 m²	10	1	0	1	1.0	156	0.857	**0.632**	-0.24	49	19

increased flux increases wall losses and internal convection losses, but not enough to overshadow the gains from reduced external area.

3.4. Areas for further work

For improved accuracy, further work should add the effect of spatially varying solar flux, the effect of paint (Pyromark or similar) coating, more accurate correlations for internal heat transfer. The performance of water (direct steam generation) would also be of interest, however complexities in the two-phase flow modelling prevented its inclusion at this stage. Finally, the present analysis did not deal accurately with the benefits of cavity-like geometries, and these are clearly a configuration of interest in industrial plants such as PS20. The effect of surface emissivity from tube banks was not handled. The effect of circumferential variations in absorbed flux and in tube temperature were not handled, and may be quite important. Rigorous optimisation of receiver design parameters should be conducted so that comparisons between alternative working fluids can be made more robustly. Minor losses were not included in the pressure drop analysis, nor were possible unshaded areas of pipework. The performance of air receivers was poor, but improvement could be possible through the addition of internal fins or porous structures on the inside of pipes. Radiative heat transfer processes (as opposed to only convective) for the inside of the pipes may become important at elevated temperatures, but were not considered.

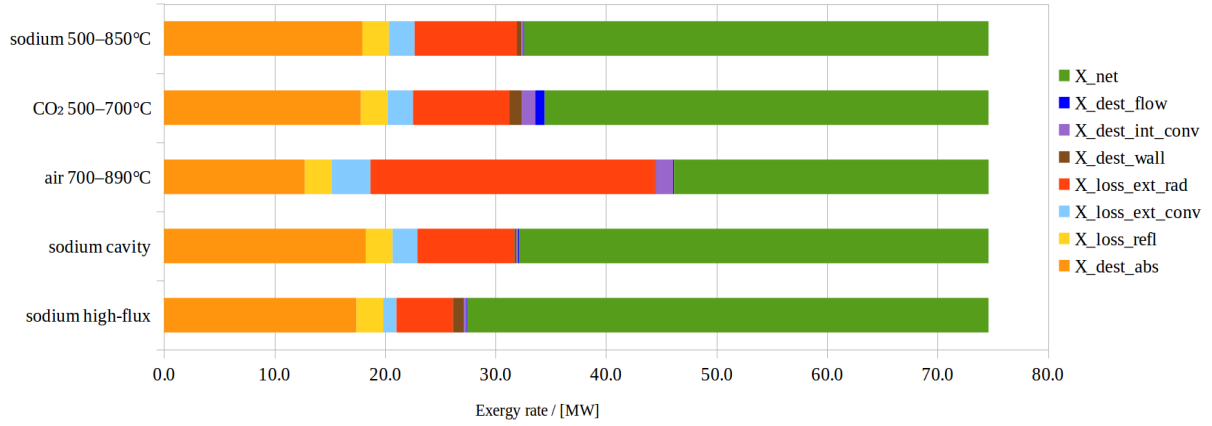

Figure 4. Case 2: In this case, the effect of increased operating temperatures are seen for sodium, CO_2 and air receivers. Next, a highly simplistic analysis of cavity receiver configuration shows very little change. Finally, the effect of a solar field with twice the concentration ratio is shown. The strong benefit in this high-flux case arises from the fact that emission losses and convection losses are reduced essentially by half due to the area change, and wall and internal convection thermal resistance do not increase to the same extent.

4.Conclusions

An analysis was presented for tubular receivers with a range of working fluids. The benefits of sodium as a receiver working fluid was evident, especially in the context of elevated temperatures and with higher-flux and/or cavity receivers. For planar receivers, the high performance of molten salt as a working fluid was confirmed. Supercritical CO_2 was seen to be quite promising, however much of the benefit of this fluid could be said to lie in the balance of plant, rather than in the receiver. Finally, air was seen to be a challenging fluid for tubular receiver applications, although with the simplified approach used here many opportunities for improvement were omitted.

Acknowledgement

This research was performed as part of the Australian Solar Thermal Research Initiative (ASTRI), a project supported by the Australian Government, through the Australian Renewable Energy Agency (ARENA). Responsibility for the views, information or advice expressed herein is not accepted by the Australian Government.

References

[1] K. Lovegrove, G. Burgess and J. Pye (2011). 'A new 500 m² paraboloidal dish solar concentrator', *Solar Energy* (85) 620-626.
[2] C. K. Ho and B. D. Iverson (2014). 'Review of high-temperature central receiver designs for concentrating solar power', *Renewable and Sustainable Energy Reviews* (29) 835 - 846.
[3] M. J. Montes, A. Abánades and J. M. Martínez-Val (2010). 'Thermofluidynamic Model and Comparative Analysis of Parabolic Trough Collectors Using Oil, Water/Steam, or Molten Salt as Heat Transfer Fluids', *Journal of Solar Energy Engineering* (132) 021001.
[4] N. Boerema, G. Morrison, R. Taylor and G. Rosengarten (2013). 'High temperature solar thermal central-receiver billboard design ', *Solar Energy* (97) 356 - 368.
[5] M. Rodríguez-Sánchez, A. Soria-Verdugo, J. A. Almendros-Ibáñez, A. Acosta-Iborra and D. Santana (2014). 'Thermal design guidelines of solar power towers', *Applied Thermal Engineering* (63) 428 - 438.
[6] C. K. Ho, A. R. Mahoney, A. Ambrosini, M. Bencomo, A. Hall and T. N. Lambert (2013). 'Characterization of Pyromark 2500 Paint for High-Temperature Solar Receivers', *Journal of Solar Energy Engineering* (136) 014502.
[7] A. B. Zavoico (2001). 'Solar Power Tower Design Basis Document', SAND2001-2100, Sandia National Laboratories, .
[8] J. Fink and L. Leibowitz (1995). 'Thermodynamic and transport properties of sodium liquid and vapor', technical report ANL/RE-95/2, Reactor Engineering Division, Argonne National Laboratories, .
[9] R. Span and W. Wagner (1996). 'A new equation of state for carbon dioxide covering the fluid region from the triple-point temperature to 1100 K at pressures up to 800 MPa', *J Phys Chem Ref Data* (26).
[10] A. Fenghour, W. A. Wakeham and V. Vesovic (1998). 'The Viscosity of Carbon Dioxide', *J Phys Chem Ref Data* (27) 31-44.
[11] V. Vesovic, W. A. Wakeham, G. A. Olchowy, J. V. Sengers, J. T. R. Watson and J. Millat (1990). 'The Transport Properties of Carbon Dioxide', *J Phys Chem Ref Data* (19) 763-808.
[12] H. Y. Lo, D. L. Carroll and L. I. Stiel (1966). 'Viscosity of Gaseous Air at Moderate and High Pressures.', *Journal of Chemical & Engineering Data* (11) 540-544.
[13] K. Kadoya, N. Matsunaga and A. Nagashima (1985). 'Viscosity and Thermal Conductivity of Dry Air in the Gaseous Phase', *Journal of Physical and Chemical Reference Data* (14) 947-970.
[14] E. W. Lemmon, M. L. Huber and M. O. McLinden (2007). 'NIST Reference Fluid Thermodynamic and Transport Properties—REFPROP Version 8.0', User's Guide, NIST, Boulder, Colorado.
[15] J. P. Holman, 2009. *Heat transfer*. McGraw-Hill, .
[16] N. Boerema, G. Morrison, R. Taylor and G. Rosengarten (2012). 'Liquid sodium versus Hitec as a heat transfer fluid in solar thermal central receiver systems ', *Solar Energy* (86) 2293 - 2305.
[17] P. F. Incropera and D. P. DeWitt, 1996. *Fundamentals of Heat and Mass Transfer*. Wiley, USA, .
[18] R. Zanino, R. Bonifetto, J. Christian, C. Ho and L. S. Richard (2014). 'Effects of RANS-type Turbulence Models on the Convective Heat Loss Computed by CFD in the Solar Two Power Tower', *Energy Procedia* (49) 569 - 578.
[19] X. Cheng and T. Schulenberg (2001). 'Heat transfer at supercritical pressures: Literature review and application to an HPLWR', scientific report FZKA 6609, Forschungszentrum Karlsruhe GmbH, Karlsruhe.
[20] J. Pacio, C. Singer, T. Wetzel and R. Uhlig (2013). 'Thermodynamic evaluation of liquid metals as heat transfer fluids in concentrated solar power plants', *Applied Thermal Engineering* (60) 295-302.
[21] T. L. Bergman, A. S. Lavine, F. P. Incropera and D. P. DeWitt, 2011. *Fundamentals of Heat and Mass Transfer*. Wiley, .
[22] Y. Candau (2003). 'On the exergy of radiation', *Solar Energy* (75) 241-247.
[23] C. Singer, R. Buck, R. Pitz-Paal and H. Müller-Steinhagen (2010). 'Assessment of Solar Power Tower Driven Ultrasupercritical Steam Cycles Applying Tubular Central Receivers With Varied Heat Transfer Media', *Journal of Solar Energy Engineering* (132) 041010.\